

RSC Advances



This is an *Accepted Manuscript*, which has been through the Royal Society of Chemistry peer review process and has been accepted for publication.

Accepted Manuscripts are published online shortly after acceptance, before technical editing, formatting and proof reading. Using this free service, authors can make their results available to the community, in citable form, before we publish the edited article. This *Accepted Manuscript* will be replaced by the edited, formatted and paginated article as soon as this is available.

You can find more information about *Accepted Manuscripts* in the [Information for Authors](#).

Please note that technical editing may introduce minor changes to the text and/or graphics, which may alter content. The journal's standard [Terms & Conditions](#) and the [Ethical guidelines](#) still apply. In no event shall the Royal Society of Chemistry be held responsible for any errors or omissions in this *Accepted Manuscript* or any consequences arising from the use of any information it contains.

Tunable Ag⁺ ion releasing from Ag@C for antibacterial and antifouling performances

Xiaoliang Yan^a, Sha Li^{b*}, Yunxiang Pan^c, Bin Xing^a, Ruifeng Li^a, Ben W.-L. Jang^d,

Xuguang Liu^{a*}

^a College of Chemistry and Chemical Engineering, Taiyuan University of Technology,
Taiyuan 030024, China

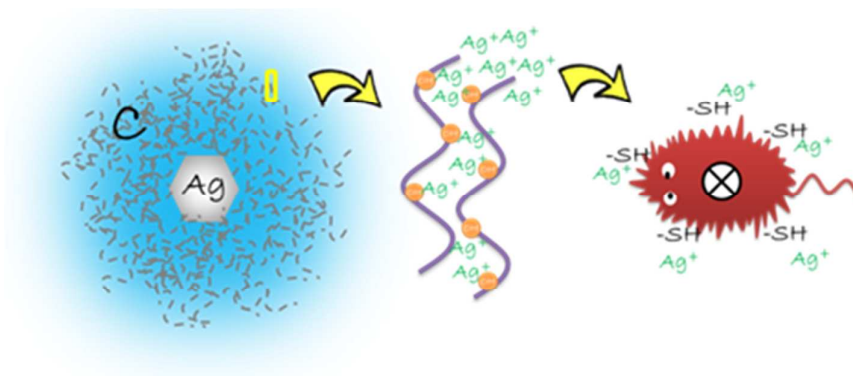
^b College of Textile Engineering, Taiyuan University of Technology,
Taiyuan 030024, China

^c School of Chemistry and Chemical Engineering, Hefei University of Technology,
Heifei 230009, China

^d Department of Chemistry, Texas A&M University-Commerce, Commerce, Texas
75429-3011, USA

*Corresponding author. Tel.: +86 351 6014138; fax: +86 351 6014138.

E-mail addresses: liuxuguang@tyut.edu.cn



A method for controllable releasing of Ag⁺ ion was proposed by synthesis of carbon-encapsulated Ag nanoparticles (Ag@C) for antibacterial and antifouling performances. Different thickness of carbon shell played a vital role in the pathways of Ag⁺ ion release. Ag@C showed a good antibacterial activity and antifouling performances.

Tunable Ag⁺ ion releasing from Ag@C for antibacterial and antifouling performances

Cite this: DOI: 10.1039/x0xx00000x

Xiaoliang Yan^a, Sha Li^{b*}, Yunxiang Pan^c, Bin Xing^a, Ruifeng Li^a, Ben W.-L. Jang^d, Xuguang Liu^{a*}

Received 00th January 2012,
Accepted 00th January 2012

DOI: 10.1039/x0xx00000x

www.rsc.org/

Silver nanoparticles have been regarded as promising candidates in the market as antibacterial agents. However, large production volume and content lead to potentially adverse effects on human health and environment, and the easy and quick exhaustion of Ag⁺ ion release causes the short-term efficacy. In this study, carbon-encapsulated Ag (Ag@C) was designed and used for antibacterial agent in view of superior antibacterial property of silver nanoparticles and tunable Ag⁺ ion releasing concentrations by different thickness of carbon shell. Structural changes were systematically investigated by a series of experimental and theoretical studies. The results showed the evolution of Ag@C originally from Ag nanoparticles then to triangular Ag nanoplates and finally to carbon-encapsulated hexagonal Ag nanoplates. The antibacterial and antifouling performances of Ag@C towards *Escherichia coli*/*Staphylococcus aureus* and *Platymonas subcordiformis*/*Tropidoneis lepidoptera* were investigated and the antibacterial mechanism was also discussed. The released Ag⁺ ion concentrations were controllable and sustainable with 39.4 and 0.667 ppb for Ag@C of the carbon shell thickness of 31.5 and 247 nm, which attenuated the toxicity of Ag nanoparticles. Ag@C showed stable antibacterial and antifouling property and proved suitable for potentially biological and environmental applications.

1. Introduction

Marine biofouling is a worldwide problem¹⁻⁵. The surface immersed in seawater suffers from the settlement of marine organisms including micro-organisms (bacteria, algae spores) and macro-organisms (barnacles, mussels). This unwanted colonization has detrimental impacts when human develop and utilize the ocean. Owing to the accumulation of biofouling on the surface of vessels, fuel consumption increases and maneuver ability impairs, leading to the cost of billions of dollars per year in transportation⁶. Up to now, using marine antifouling coating is the most effective way for avoiding marine organism attachment.

Generally, according to the toxicity of coating materials, the antifouling strategies can be divided into two main categories, nontoxic coating and chemically active coating. The first approach uses nature-inspired structure to inhibit the settlement of organisms without involving chemical reactions. Microtopographical surface (marine animal skins) and superhydrophobic surface have been employed to defend against biofouling by controlling surface wettability and reducing surface energy. This method disrupts physically the bioadhesion of marine organisms. However, antifouling property of this coating will be gradually deteriorated for long time usage under real marine environment^{7,8}. Chemically active coating limits the settlement of marine organism by chemically active compounds. In the last century, tributyltin (TBT) was used as the most popular antifouling agent. TBT causes serious

damage to the food chain, and the International Maritime Organization (IMO) has forbidden TBT-based agent in marine antifouling coatings. Thus, the development of environmental-friendly antifouling agent is in urgent.

Silver has been extensively designed and well known as a bacteriostatic agent in the treatment of infectious diseases since ancient time. Silver nanoparticles have a broad-spectrum and long-term antibacterial activity and also exhibit low toxicity towards mammalian cells at a small concentration^{9,10}. Researchers used silver nanoparticles to inhibit marine organisms¹¹⁻¹⁵. However, there are some disadvantages limiting this antifouling material for further development: (i) large production volume and content which lead to potentially adverse effects on human health and environment, (ii) short-term efficacy which results from the exhaustion of Ag⁺ ion release, (iii) poor compatibility with resin which decreases the uniformity. Based on these facts, the preparation of highly stable Ag nanoparticles with controllable and sustainable Ag⁺ ion release is a prerequisite for a promising bacteriostatic agent with low toxicity and long-term activity.

Core-shell structural Ag nanocomposites can meet the demands. Many efforts have been made to synthesize core-shell Ag@silica due to its synergetic effects of core Ag and shell materials for antibacterial and antifouling investigation¹⁶⁻²⁰. Besides, carbon nanoscrolls filled with Ag nanoparticles were prepared by sonication and possessed enhanced and lengthened antifungal activity²¹. The combination of graphene oxide (GO)

with Ag@Fe₂O₃ enhanced the stability of Ag nanoparticles and slowed down the Ag⁺ ion release rate²². Ag@Fe₂O₃-GO showed better long-term antibacterial activity than that of plain Ag and Ag@Fe₂O₃. Therefore, the introducing of auxiliary materials for controlling Ag⁺ ion release is necessary. Carbon materials have been regarded as promising candidates for Ag encapsulating materials owing to their fine physical/chemical durability and good biological compatibility. Firstly, carbon shell will improve environmental stability of Ag nanoparticles by protecting them from light and moisture. Then, Ag⁺ ion sustained-release can be controlled by the tunable thickness of carbon shell, leading to the long-term antifouling stability. Finally, carbon shell can be functionalized and chemically bonded with resin, which can improve the dispersity of Ag nanoparticles.

In this work, tunable carbon shell encapsulated Ag (Ag@C) nanocomposite was synthesized by changing the hydrothermal reaction time. The growth mechanism of Ag@C was proposed based on the experimental and theoretical study. The general objective of this study is to control Ag⁺ ion release concentration by the different carbon shell thickness, and effectively reduce the influence to the environment. The antibacterial activity (long-term stability) together with antifouling property was studied. To our best knowledge, this kind of nanocomposite has not been reported for antibacterial and algal inhibiting performances. Antibacterial mechanism of Ag@C was also discussed.

2. Experimental

2.1. Materials

Glucose, silver nitrite (AgNO₃), acetone, and ethanol were commercially available (Tianjin Kemiou Chemical Agent Factory) and of analytical grade without further purification. Algal medium (f/2 seawater medium) was purchased from Shanghai LeadingTec company.

2.2. Preparation of Ag@C

Ag@C core-shell structural nanocomposite was prepared by hydrothermal method²³. In a typical procedure, AgNO₃ aqueous solution (0.05 mol L⁻¹, 15 mL) was added drop by drop into the glucose solution (0.1 mol L⁻¹, 15 mL) under vigorous stirring. The mixture was ultrasonicated for 10 minutes. Finally, the above-mentioned solution was sealed in a 50 mL Teflon-sealed autoclave. The autoclave was kept at 180 °C for 1~16 h before being cooled in air naturally. After that, the sample was obtained by centrifuging. Three times of centrifugation/washing/redispersion procedures in acetone, deionized water and alcohol were required before oven drying at 50 °C in vacuum. The obtained products were denoted by the composition and reaction time. Therefore, Ag@C-8 and Ag@C-16 correspond to the Ag and carbon composite obtained from 8 and 16 h reaction, respectively.

2.3. Characterizations

Transmission electron microscopy (TEM) observations were carried out using JEM100CXII operated at 100 kV (a small quantity of samples ethanol solution was dropped onto the 300 mesh copper TEM grid). Scanning electron microscopy (SEM) images (powder samples) with energy dispersive X-ray spectra (EDS) were recorded with Hitachi field emission scanning electron microscope (S4800). Diffuse-reflectance UV-Vis (DR UV-Vis) spectra were recorded with a Shimadzu UV-2550 spectrophotometer (three times dilute supernate of samples after hydrothermal process). X-ray diffraction (XRD) analyses were performed with a Rigaku D/MAX-2500 V/PV using Cu-K α radiation (40 kV and 200 mA) at a scanning speed of 4°/min over the 2 θ range of 10°-80° (powder samples). Raman

spectroscopy was used to estimate the presence of carbon and silver species. Spectra were collected with a DXR Microscope instrument using a laser with 532 nm wavelength for excitation (powder samples). Fourier transform infrared (FT-IR) spectra were recorded using a Tensor 27 spectrometer (Bruker) with a resolution of 4 cm⁻¹ (powder samples with KBr pellet). Thermogravimetric analysis (TGA) was carried out using a Netzsch STA 449 F3 system with a heating rate of 10 °C min⁻¹ (from 100 °C to 600 °C) under flowing air (25 mL min⁻¹). Zetasizer NanoZS90 (Malvern Instruments Ltd., UK) was used to measure and calculate the ζ -potential value of Ag@C solution in water. The Ag⁺ ion concentration of each sample was quantitatively determined by inductively-coupled plasma mass spectrometry (ICP-MS, Thermo X series 2).

2.4. Antibacterial tests

Two representative bacteria *Escherichia coli* (*E. coli*) and *Staphylococcus aureus* (*S. aureus*) corresponding to gram-negative and gram-positive bacteria were selected as the indicators for antibacterial evaluation. Bacteria were grown in a nutrient agar culture medium (peptone 10 g, beef extract 3 g, NaCl 3 g, distilled water 1000 mL, pH 7.4) and incubated overnight at 37 °C. Then, a culture where bacteria grew in a logarithmic growth phase (18 h) was prepared for an antibacterial test. All disks and materials were sterilized in an autoclave at 120 °C for 30 min before tests. The antibacterial activities of Ag@C samples were performed by disk diffusion assay. The procedure of disk diffusion assay included: (i) placing a 5 mm disk saturated with 20 μ L of Ag@C composite aqueous dispersion (500 μ g μ L⁻¹) onto an agar plate seeded with *E. coli* or *S. aureus*; (ii) measuring the diameters of the inhibition zones after incubation for 12 h at 36.8 °C.

2.5. Algal inhibiting test

Platymonas subcordiformis (*P. subcordiformis*) and *Tropidoneis lepidoptera* (*T. lepidoptera*) were selected as the indicators for antifouling evaluation. Algae were placed in the f/2 seawater (filtered by 0.4 μ m microporous membrane) medium and cultured at 20 °C with 3000 lx illumination in the shaking bed. Finally, antifouling agents were added, and the performances were observed under microscope after 24 h.

2.6. Computational methods

Geometry optimization and frequency calculations were performed by using density functional theory (DFT) as Vienna ab simulation package (VASP)²⁴. The surface was modeled by a periodic slab containing four atomic layers with full relaxation of the uppermost two layers. The p (2 × 2) unit cell was used in this study, which means the coverage of adsorbates and pre-adsorbed carbon atom is 1/4 monolayer (ML). The Monkhorst-Pack meshes of 3 × 3 × 1 K point sampling in the surface Brillouinzone were used²⁵. The optimized lattice constant of 4.18 Å is used for Ag.

3. Results and Discussion

3.1. Preparation of Ag@C

TEM observations were conducted to visually illustrate the procedure of Ag@C growth. Fig. 1 presented the morphology evolution of the as-prepared products in the hydrothermal process. Quasi-spherical Ag nanoparticles were obtained at 1 h (Fig. 1a). These Ag nanoparticles had the average size of ~20 nm. Approximately 50-60 nm triangular Ag nanoplates were observed at 2 h (Fig. 1b). After 4 h (Fig. 1c), thin carbon layer adhered onto truncated triangular Ag nanoplates, covered the outer surface and formed a shell of ~3.3 nm. Well structured carbon-encapsulated hexagonal Ag nanoplates (Fig. 1d-f) were observed at 8 and 16 h. The spot points (electron diffraction analysis of an individual Ag nanoplate locating flat on the

substrate) with a hexagonal arrangement (Fig. 1e) clearly indicated that the particle was a single crystal with its [111] orientation paralleled to the electron beam. The size of core Ag nanoplates (Ag@C-8 and Ag@C-16) remained at ~ 120 nm, unrelated with the increase of reaction time. However, the thickness of carbon shell grew from 31.5 to 247 nm, closely correlated with the prolonging of the reaction time.

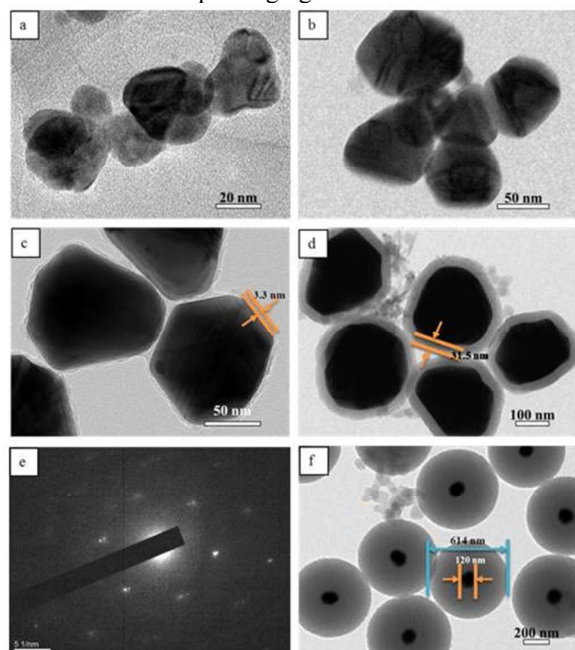


Fig. 1. TEM images of Ag@C at different reaction times: 1 h (a), 2 h (b), 4 h (c), 8 h (d), 16 h (f) and SAED of Ag@C at 8 h (e).

The overall morphology and dispersity of as-prepared Ag@C products (reaction at 8, 16 h) were further characterized by SEM in Fig. 2. It can be clearly seen in Fig. 2a that hexagonal Ag@C-8 nanoplates well scattered on the substrate. This nanocomposite possessed uniform shape and was highly dispersed. This was attributed to the presence of carbon shell acting as a barrier and preventing Ag from agglomerating. Furthermore, EDS elemental mapping of Ag@C-8 was collected, as shown in Fig. 2c-f, revealing that the Ag@C-8 consisted of Ag, C, and O elements. Obviously, the blue Ag core was surrounded by the red carbon material and green O. The results were well in consistency with TEM observations. Fig. 2b presented the SEM images of the product from 16 h reaction. It was difficult to distinguish the morphology of core Ag from the overall spherical particles, due to the thickness of carbon shell. However, based on the results of TEM observation, it was reasonable to assure that these spherical nanoparticles (~ 600 nm) were assigned to the core-shell structural nanocomposite.

UV-Vis spectra of all solutions from 1, 2, 4, and 8 h reaction before centrifugation were shown in Fig. 3. It is well-known that the plasmon resonance of nano-structured Ag was sensitive to shape, size, and morphological conversion. According to Mie theory, small spherical Ag nanocrystals exhibited a single surface plasmon band; whereas anisotropic particles showed two or three bands, depending on their shape²⁶. In Fig. 3a, the extinction spectrum of the product from 1 h showed a strong band with a maximum at 418 nm. This was characterized for typical surface plasmon resonance of silver nanoparticles²⁷, indicating that the reduction of silver ions occurred. For the 2 h

reaction product, the absorption spectrum displayed a broad band at 450 nm, together with one weak band at 330 nm. This was ascribed to the presence of triangular Ag nanoplates. It has been widely accepted that the bands at 340 and 470 nm correspond to the plasmon resonance of triangular Ag nanoplates^{28, 29}. This blue shift of the bands from 340 to 330 nm, and from 470 to 450 nm was attributed to the following two aspects: (i) the smaller size of triangular Ag nanoplates (~ 50 -60 nm in this work, while 90 nm in Ref.²⁸); (ii) the evolution of triangular Ag nanoplates into truncated Ag nanoplates³⁰. In addition, a new band emerged at 295 nm, due to the presence of carbon-containing species (carbon dot)³¹.

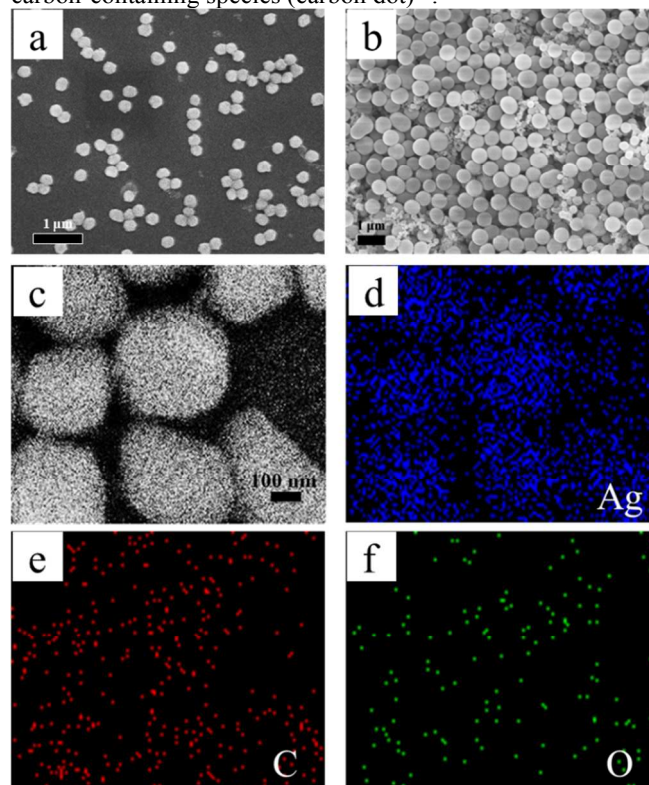


Fig. 2. SEM images of Ag@C at different reaction times: 8 h (a), 16 h (b), and FESEM EDS mapping of Ag@C at 8 h (c-f).

As the reaction proceeded to 4 h, a quite different UV-Vis spectrum was observed. Absorption spectrum exhibited three bands at 340, 368, and 492 nm. These three bands can be classified as the formation of hexagonal Ag nanoplates^{28, 32}. The weak band at 340 nm was assigned to the out-of-plane quadrupole resonance of silver nanoplates. A shoulder band with medium intensity at 368 nm was credited to the out-of-plane dipole resonance of silver nanoplates. A distinctive band (strong intensity) at 492 nm was assigned to the in-plane dipole resonance of silver nanoplates. Thus, it was confirmed that the triangular Ag nanoplates became truncated to evolve into hexagonal Ag nanoplates. Furthermore, in comparison with the absorption spectrum in Fig. 3b for 2 h reaction product, the band intensity of carbon species was enhanced for the product obtained at 4 h based on the calculation of the intensity ratio of the bands between carbon and Ag product. This probably indicated the formation of relatively large amount of carbon species on the surface of hexagonal Ag nanoplates. After reaction for 8 h (Fig. 3d), the bands eventually disappeared from the visible regime. Only one clear band at 311 nm remained. It can be deduced that one group of nano-structural

Ag was formed surrounding by a great number of carbon shell. These findings allow us to draw some conclusions about the formation and evolution of Ag@C: (i) the glucose solution can reduce the silver nitrate, and the shape of Ag changed from nanoparticles to triangular nanoplates then to hexagonal nanoplates; (ii) the remaining glucose (after the process of reduction of silver precursor) adhered and carbonized on the surface of Ag, leading to the formation of carbon-encapsulated Ag.

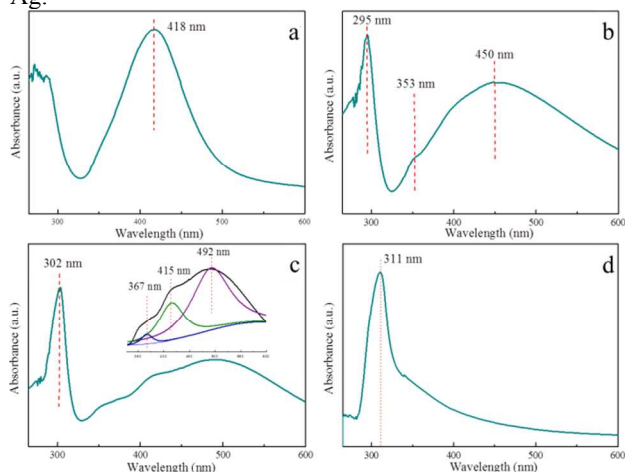


Fig. 3. UV-Vis curves of Ag@C at different reaction times: 1 h (a), 2 h (b), 4 h (c), 8 h (d).

XRD patterns of Ag@C obtained from 4, 8, and 16 h reaction were shown in Fig. 4a. It can be observed that the crystal phase of the samples was composed of carbon and silver. Diffraction peaks observed at $2\theta = 38.2^\circ$, 44.4° and 64.6° , were indexed to Ag (111), Ag (200) and Ag (220), which was well agreed with the reported values from the Joint Committee on Powder Diffraction Standards card (JCPDS, No. 04-0783). The residual board peak at 2θ degree of 25.2° corresponded to (002) crystal plane of carbon. This suggested the presence of graphite carbon with low crystallinity.

Fig. 4b showed the Raman spectra of Ag@C obtained from 4, 8, and 16 h reaction. The Raman spectrum of as-obtained sample from 4 h presented typical bands of Ag (four bands at 556 , 842 , 987 and 1071 cm^{-1}).³³ One weak band at 1580 cm^{-1} was assigned to the G peak of carbon. The band intensity of Ag was greatly larger than that of carbon. With increasing reaction time, the band intensity of Ag dramatically decreased even disappeared, while the band intensity of carbon significantly increased. Additional band at 1380 cm^{-1} (disorder-induced D peak) emerged with the increasing of reaction time, implying the low crystallinity of carbon.

3.2. Characterizations of Ag@C-8 and Ag@C-16

The surface properties (functional groups) and thermal stability (Ag loading content) of Ag@C were studied using FT-IR and TGA. Fig. 5a illustrated the FT-IR spectra of Ag@C-8 and Ag@C-16. The band centered at ~ 3500 cm^{-1} was ascribed to the single bond -OH stretching vibrations. The signature bands at 1700 and 1615 cm^{-1} corresponded to C double bond, caused by the aromatization of glucose during the hydrothermal treatment. The absorption bands from 1000 to 1300 cm^{-1} were attributed to the C single bond -OH stretching and -OH bending vibrations, suggesting the existence of large numbers of residual hydroxyl groups. Partially dehydrated residues in which reductive -OH and -CHO were covalently bonded to the carbon frameworks improved the hydrophilicity and stability of the nanospheres in aqueous systems, and would greatly expand

their potential application range in biochemistry, diagnostics, and drug delivery.

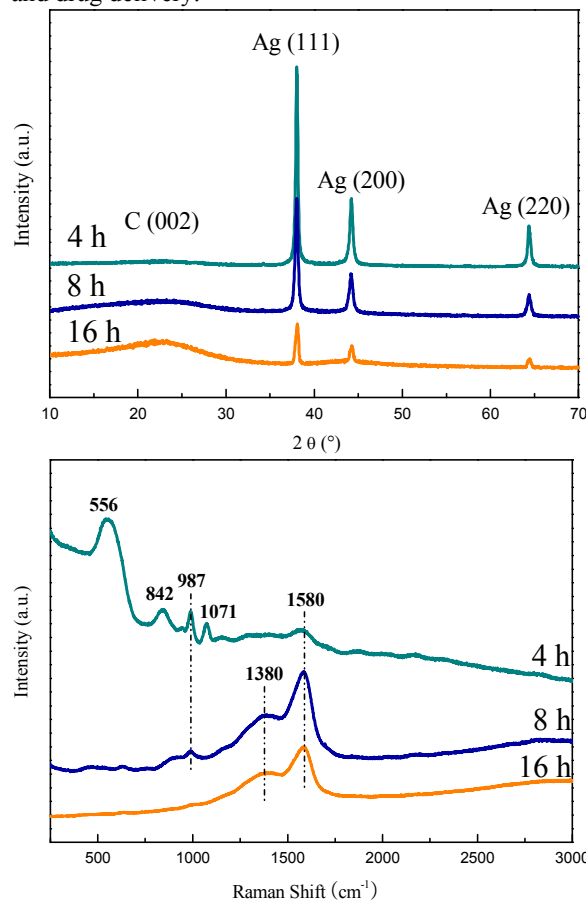


Fig. 4. XRD patterns (a) and Raman spectra (b) of Ag@C at 4 h, 8 h, and 16 h.

Fig. 5b showed the TG-DTA profiles of Ag@C-8 and Ag@C-16. The profiles of both samples exhibited one obvious stage of weight loss as a result of the combustion of carbon. The weight loss of Ag@C-16 was greater in comparison with that of Ag@C-8. Furthermore, the DTA peak of Ag@C-16 (449 $^\circ\text{C}$) shifted to a higher temperature compared with that of Ag@C-8 (389 $^\circ\text{C}$). This was mainly ascribed to the large amount of carbon gained with increasing reaction time, leading to higher combustion temperature of carbon. The remaining weight percentage (Ag loading content) of Ag@C-8 and Ag@C-16 was 30.2% and 13.3% , respectively. This suggested that Ag@C-8 had a higher Ag loading content.

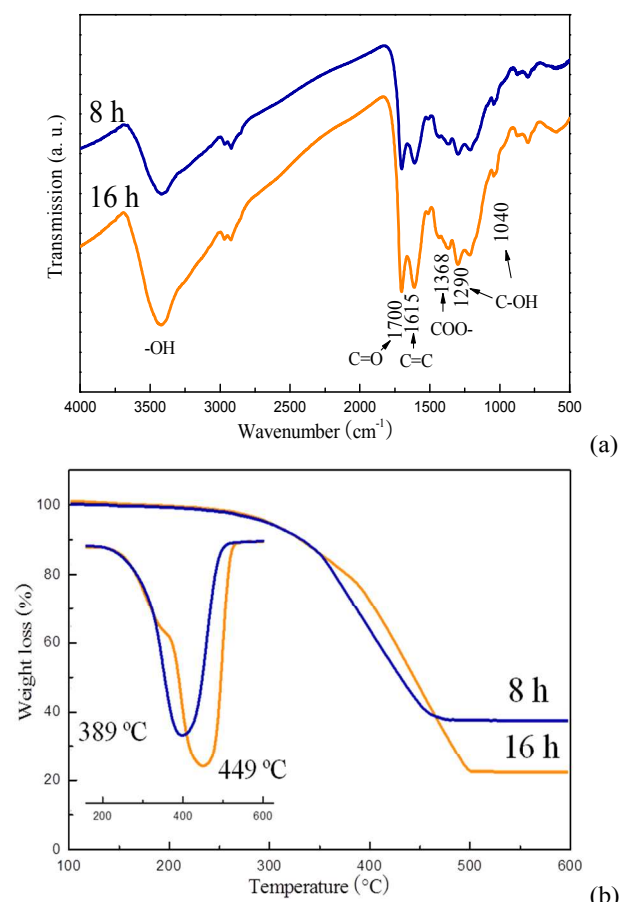


Fig. 5. FT-IR spectra (a) and TG-DTA profiles (b) of Ag@C-8 and Ag@C-16.

3.3. Mechanism of formation of Ag@C

According to the results of TEM, SEM, UV-Vis, XRD and Raman characterizations, the growth model for Ag@C was proposed in Fig. 6a. At the very beginning, the reduction of silver ions by glucose occurred, leading to the thermodynamically favorable formation of Ag nanoparticles. These nanoparticles had structural defects, as was shown in Fig. 1a. While the intermediate state (formation of Ag nanoparticles) was unstable, these nanoparticles would grow large or evolve into anisotropic morphology within the scope of kinetic control. As the reaction proceeded, these Ag nanoparticles grew larger and evolved into Ag triangular nanoplates. Xia and co-workers reported a kinetically controlled synthesis of Ag triangular nanoplates using mild reducing reagent PVP³⁴. With a slow reduction rate, the nucleation and growth of Ag was in a kinetic control region. While a fast reduction rate led to the growth of other structures instead of nanoplates. Also, they pointed out the significant influence of structural defects in the formation of nanoplates. The presence of defects in the initial seed played an important role in the anisotropic growth of triangular nanoplates³⁵. Thus, in this work the morphology transformation of Ag nanoparticles into Ag triangular nanoplates was caused by the structural defects of Ag nanoparticles and the kinetically controlled reduction of Ag species by glucose.

These Ag triangular nanoplates became truncated and evolved into hexagonal Ag nanoplates. In order to explain the morphology change of Ag nanoplates, DFT was applied to investigate the binding energies of atomic C on Ag (111) and Ag (100) facets, separately. Ag surfaces were modeled with a

periodic array of four-layer-thick slabs. The interaction models of atomic C with Ag (111) and Ag (100) were shown in Fig. 6b. The adsorption energy (E_{ads}) is calculated by formula:

$E_{ads} = E_{A/M} - E_A - E_M$. E_A , E_M , and $E_{A/M}$ mean the calculated energy of adsorbate, substrate, adsorption system, respectively.

The calculated results showed that atomic C prefers to adsorb at the hollow site, even their original adsorb sites were top or bridge. The calculated adsorption energies of atomic C on Ag (100) and Ag (111) were -4.41 eV and -3.33 eV, respectively. This indicated that the carbon from glucose decomposition could prefer to interact with the Ag (100) surface, and could inhibit the growth of the surface. As a result, the growing of the sample along the (100) direction stopped by the deposited carbon and forms a step structure. As for the Ag (111) surface, due to the relatively weak interaction between the surface and the carbon atoms, Ag atoms can easily enter into the interface between the surface and the carbon atoms. This may help the growth of the Ag (111) surface. Owing to the excess amount of glucose, the as-obtained hexagonal Ag nanoplates were encapsulated by carbon shell through the carbonization of glucose.

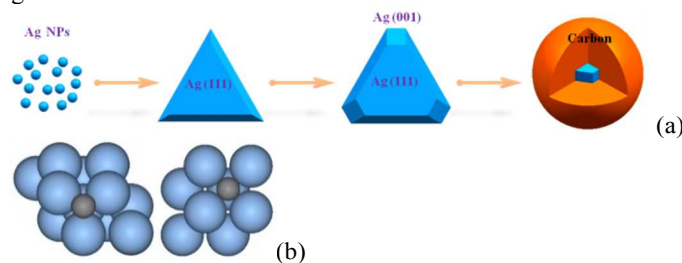


Fig. 6. (a) The growth mechanism of Ag@C. (b) The interaction model atomic carbon with Ag crystal planes: Ag (111) (left) and Ag (100) (right).

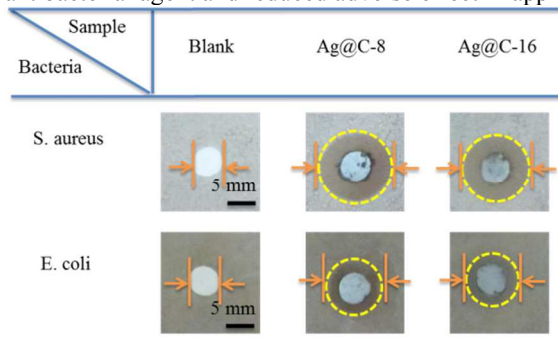
3.4. Antibacterial property of Ag@C

The antibacterial activities of Ag@C-8 and Ag@C-16 were evaluated by determining the presence of inhibition zones. The antibacterial agent was used in water solution, and the stability of the solution was analyzed by the ζ -potential analysis. The ζ -potential value of Ag@C in water (100 ppm) was measured. The value was large and negative (-45.0 mV), indicating the stable of the solution. Antibacterial effects in the form of inhibition zones, assessed by the disk diffusion of the Ag@C-8 and Ag@C-16, were shown in Fig. 7a. As expected, the normal growth of *E. coli* and *S. aureus* was seen in the agar plate when no composites were introduced. The blank experiment with only filter paper demonstrated almost no antibacterial activity without the addition of Ag@C. Both Ag@C-8 and Ag@C-16 performed relatively strong antibacterial activity, as depicted from the inhibition zone. The diameters of inhibition zone from Ag@C-8 and Ag@C-16 on *S. aureus*/*E. coli* were 13.2/11.8 mm and 10.4/9.3 mm, respectively. It can be seen that Ag@C-8 exhibited better antibacterial performance than Ag@C-16. The antibacterial activity for the repeated use of Ag@C was investigated (Fig. 7b). The diameters of inhibition zone from Ag@C-8 and Ag@C-16 were almost unchanged, indicating the stable antibacterial activity.

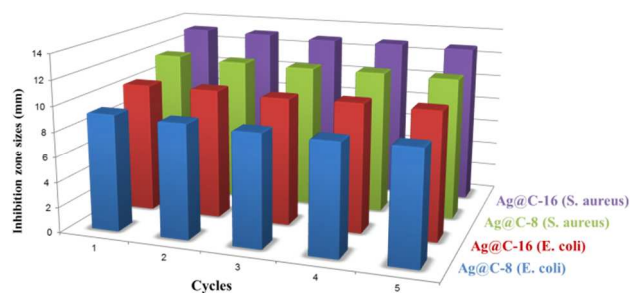
The antibacterial mechanism of Ag nanoparticles has not been fully understood. However, many studies demonstrated that the released Ag^+ ion from Ag nanoparticles plays a crucial role in antibacterial performance^{14-22, 36}. Hurt and co-workers have reported that Ag^0 nanoparticles would not be persistent in realistic environmental compartments containing dissolved oxygen through thermodynamic analysis and kinetic

measurements. H^+ and dissolved O_2 oxidized Ag nanoparticles to release Ag^+ ion³⁶. When Ag@C acted as the antifouling agent in seawater, Ag^+ ion released from the Ag core, and penetrated through the carbon shell to contact with fouling organisms. Ag^+ ion concentrations of Ag@C-8 and Ag@C-16 in water (the above reference mentioned sea salts had only a minor effect on dissolved silver release) were tested by ICP-MS. Fig. 8a showed the Ag^+ ion release profiles of Ag@C-8 and Ag@C-16. The released Ag^+ ion concentrations were 39.4 and 0.667 ppb for Ag@C-8 and Ag@C-16, respectively, in the first run and subsequently maintained at these levels during the five-cycle test. These concentrations were below the standards of US Environmental Protection Agency (US EPA) and World Health Organization (WHO) for drinking water (54 ppb)³⁷. The cytotoxicity of the Ag@C particle needs to be clarified by the presence of outer carbon shell, which is attributed to the fact that Ag particles were wrapped by carbon shell. Similarly, by using the hydrothermal approach carbon spheres were obtained³⁸. The resultant carbon nanospheres showed low cytotoxicity and when the concentration increased to $100 \mu g mL^{-1}$, the cell viability remained above 65%. Furthermore, the studies on the effects of carbon-coated ZnO nanorods and pure ZnO nanorods on cultured mouse fibroblast cells revealed that the coating of biocompatible carbon remarkably reduced the cytotoxicity of ZnO nanorods³⁹.

Fig. 8b was used to illustrate the antibacterial process of Ag@C. Ag@C had abundant pores and the channels, which supplied the route for Ag^+ ion penetration. Hydroxyl inherited from glucose, has been grafted on the channels after hydrothermal treatment, which was beneficial to adsorb Ag^+ ion, making the pores of Ag@C as Ag^+ ion reservoir. Then the dissolved Ag^+ ion bounded to thiol groups in protein and interfered with DNA replications, inducing the inactivation of the bacterial proteins. With the consumption of Ag^+ ion by bacteria, the fresh Ag^+ ion was replenished. The thickness of carbon shell was a dominant factor for tuning Ag^+ ion release. The thickness of the shell determined the pathways of Ag^+ ion release. The thicker shell of Ag@C-16 (247 nm, Fig. 1f) than that of Ag@C-8 (31.5 nm, Fig. 1d) contributes to the longer pathways, leading to significantly delaying of the diffusion rate of Ag^+ ion. Meanwhile, hydroxyl was in direct proportion to the thickness of the shell. Ag@C-16 had a larger density of carbon shell, which produced plentiful amounts of hydroxyl and reserved a great deal of Ag^+ ion. If 100 ppm of Ag@C solution was employed, the complete exhausting of Ag^+ ion over Ag@C-8 would be lasted for about 2 years and almost 55 years for Ag@C-16. Thus, Ag@C (especially Ag@C-16) possessed continuous and controllable release feature, which was the fundamental character of stable, long-term efficiency as antibacterial agent and reduced adverse effect in application.



(a)

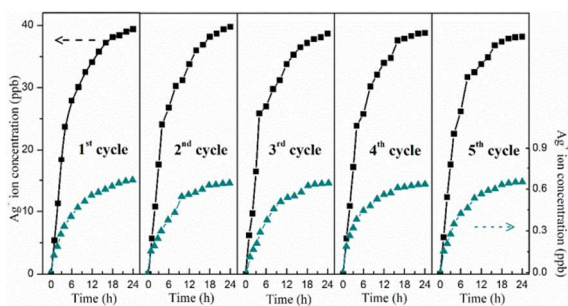


(b)

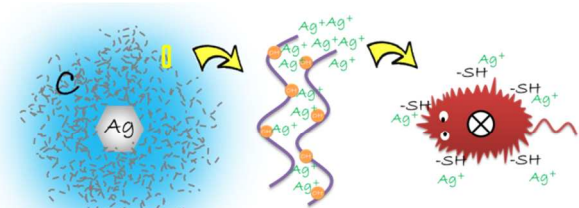
Fig. 7. (a) The inhibition zone test for *S. aureus* and *E. coli* of blank, Ag@C-8 and Ag@C-16. (b) Antibacterial activity for repeated use of Ag@C.

3.5. Algal inhibiting property of Ag@C

Platymonas subcordiformis (*P. subcordiformis*) and *Tropidoneis lepidoptera* (*T. lepidoptera*) in seawater were selected as representative microalgae, in order to fully evaluate the practical use Ag@C as antifouling material. Fig. 9 exhibited the microscopic photos for algal inhibiting property. In fresh seawater, *P. subcordiformis* was a type of active (Fig. 9) and motile (Movie S1) green alga; whereas *T. lepidoptera* can be firmly adhered and settled to the substrate surface. Much less *P. subcordiformis* was observed on 100 ppm Ag@C-8 and Ag@C-16 (Movie S2). Additionally, with the Ag content to 300 ppm, a large portion of *T. lepidoptera* was inhibited and killed, as can be seen from the empty area in Fig. 9, by Ag@C-8 and Ag@C-16. The results were in accordance with the stable performance and long-term efficiency of antibacterial behavior.



(a)



(b)

Fig. 8. (a) The Ag^+ ion release rate of Ag@C-8 (■) and Ag@C-16 (▲). (b) Schematic of antibacterial process of Ag@C.

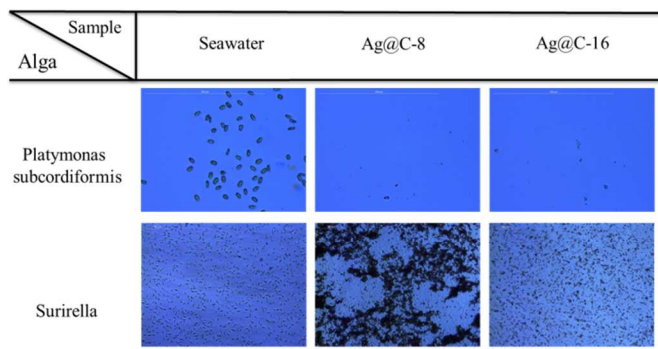


Fig. 9. The fluorescence microscope photos for *P. subcordiformis* (100 ppm antifouling agent) and *T. lepidoptera* (300 ppm antifouling agent) of blank, Ag@C-8 and Ag@C-16 test.

4. Conclusions

In summary, a method for controllable releasing of Ag^+ ion was proposed by synthesis of carbon-encapsulated Ag nanoparticles for antibacterial and antifouling performances. Experimental and theoretical studies demonstrated the growth procedure of Ag nanoparticles to Ag triangular nanoplates further to carbon-encapsulated hexagonal Ag nanoplates. Different thickness of carbon shell played a vital role in the pathways of Ag^+ ion release. Ag@C showed a good antibacterial activity and antifouling performances towards *E. coli*/*S. aureus* and *P. subcordiformis*/*T. lepidoptera*, respectively. Besides, Ag@C exhibited low released Ag^+ ion concentrations below the standards of US EPA and WHO for drinking water. The results showed that core-shell structural Ag@C gave new opportunities for antibacterial and antifouling materials with high efficient, low toxicity, and long-term stability. Furthermore, this method for the tunable releasing of Ag^+ ion can be used for other metal ions controllable releasing.

Acknowledgements

The authors thank financial supports from National Natural Science Foundation of China (21406153) and Shanxi Province Science Foundation for Youths (2014021014-2). The authors also thank the help of antifouling performance by China Shipbuilding Industry Corporation (No. 725 Institute in Xiamen City).

Notes and references

a College of Chemistry and Chemical Engineering, Taiyuan University of Technology, Taiyuan 030024, China; b College of Textile Engineering, Taiyuan University of Technology, Taiyuan 030024, China; c School of Chemistry and Chemical Engineering, Hefei University of Technology, Hefei 230009, China; d Department of Chemistry, Texas A&M University-Commerce, Commerce, Texas 75429-3011, USA.

*Corresponding author. Tel.: +86 351 6014138; fax: +86 351 6014138.

E-mail addresses: luxuguang@tyut.edu.cn; yanxiaoliang@tyut.edu.cn

Electronic Supplementary Information (ESI) available: [details of any supplementary information available should be included here]. See DOI: 10.1039/b000000x/

References:

- J. A. Callow, M. E. Callow, *Nat. Commun.*, 2011, **2**, 244-254.
- M. Lejars, A. Margailan, C. Bressy, *Chem. Rev.*, 2012, **112**, 4347-4390.

- C. F. Ma, L. G. Xu, W. T. Xua, G. Z. Zhang, *J. Mater. Chem. B*, 2013, **1**, 3099-3106.
- A. K. Singh, P. Singh, S. Mishra, V. K. Shahi, *J. Mater. Chem.*, 2012, **22**, 1834-1844.
- P. M. Imbesi, N. V. Gohad, M. J. Eller, B. Orihuela, D. Rittschof, E. A. Schweikert, A. S. Mount, K. L. Wooley, *ACS Nano*, 2012, **6**, 1503-1512.
- M. P. Schultz, J. A. Bendick, E. R. Holm, W. M. Hertel, *Biofouling*, 2011, **27**, 87-98.
- A. J. Scardino, R. de Nys, *Biofouling*, 2010, **27**, 73-86.
- L. D. Chambers, K. R. Stokes, F. C. Walsh, R. J. K. Wood, *Surf. Coat. Technol.*, 2006, **201**, 3642-3652.
- J. Kusnetsov, E. Iivanainen, N. Elomaa, O. Zacheus, P. J. Martikainen, *Water Res.*, 2001, **35**, 4127-4225.
- Z. Z. Li, L. J. Fan, T. Zhang, K. Li, *J. Hazard. Mater.*, 2011, **187**, 466-472.
- T. S. Sileika, H.-D. Kim, P. Maniak, P. B. Messersmith, *ACS Appl. Mater. Interfaces*, 2011, **3**, 4602-4610.
- P. Gunawan, C. Guan, X. H. Song, Q. Y. Zhang, S. S. J. Leong, C. Tang, Y. Chen, M. B. Chan-Park, M. W. Chang, K. Wang, R. Xu, *ACS Nano*, 2011, **5**, 10033-10040.
- T. Q. Tuan, N. V. Son, H. T. K. Dung, N. H. Luong, B. T. Thuy, N. T. V. Anh, N. D. Hoa, N. H. Hai, *J. Hazard. Mater.*, 2011, **193**, 1321-1329.
- M. S.-L. Yee, P. S. Khiew, Y. F. Tan, Y.-Y. Kok, K. W. Cheong, W. S. Chiu, C.-O. Leong, *Colloid Surf. A: Physicochem. Eng. Aspects*, 2014, **457**, 382-391.
- D. Inbakandan, C. Kumar, L. Stanley Abraham, R. Kirubakaran, R. Venkatesan, S. Ajmal Khan, *Colloids Surf. B: Biointerfaces*, 2013, **111**, 636-643.
- P. Saint-Cricq, J. Z. Wang, A. Sugawara-Narutaki, A. Shimojima, Tatsuya Okubo, *J. Mater. Chem. B*, 2013, **1**, 2451-2454.
- C. Durucan, B. Akkopru, *J. Biomed. Mater. Res. B Appl. Biomater.*, 2010, **93**, 448-458.
- G. Fuertes, O. L. Sánchez-Muñoz, E. Pedrueza, K. Abderrafi, J. Salgado, E. Jiménez, *Langmuir*, 2011, **27**, 2826-2833.
- S. K. Das, M. M. R. Khan, T. Parandhaman, F. Laffir, A. K. Guha, G. Sekaran, A. B. Manda, *Nanoscale*, 2013, **5**, 5549-5560.
- X. S. Zhang, J. X. Wang, K. Xu, Y. Le, J. F. Chen, *J. Nanosci. Nanotechnol.*, 2011, **11**, 3481-3487.
- C. Li, X. S. Wang, F. Chen, C. L. Zhang, X. Zhi, K. Wang, D. X. Cui, *Biomaterials*, 2013, **34**, 3882-3890.
- N. Gao, Y. J. Chen, J. Jiang, *ACS Appl. Mater. Interfaces*, 2013, **5**, 11307-11314.
- X. M. Sun, Y. D. Li, *Langmuir*, 2005, **21**, 6019-6024.
- G. Kresse, D. Joubert, *Phys. Rev. B*, 1999, **59**, 1758-1775.
- H. J. Monkhorst, J. D. Pack, *Phys. Rev. B*, 1976, **13**, 5188-5192.
- G. Mie, *Ann. Phys.*, 1908, **25**, 377-445.
- J. J. Mock, M. Barbic, D. R. Smith, D. A. Schultz, S. Schultz, *J. Chem. Phys.*, 2002, **116**, 6755-6759.
- R. C. Jin, Y. W. Cao, C. A. Mirkin, K. L. Kelly, G. C. Schatz, J. G. Zheng, *Science*, 2001, **294**, 1901-1903.
- J. Yang, Q. B. Zhang, J. Y. Lee, H.-P. Too, *J. Collid. Inter. Sci.*, 2007, **308**, 157-161.
- S. H. Chen, D. L. Carroll, *NanoLett.*, 2002, **2**, 1003-1007.

ARTICLE

- 31 Q. L. Wang, H. Z. Zheng, Y. J. Long, L. Y. Zhang, M. Gao, W. J. Bai, *Carbon*, 2011, **49**,3134-3140.
- 32 J. An, B. Tang, X. H.Ning, J. Zhou, S. P. Xu, B. Zhao, W. Q. Xu, C.Corredor, J. R. Lombardi, *J. Phys. Chem. C*, 2007, **111**, 18055-18059.
- 33 G. I. N. Waterhouse, G. A. Bowmaker, James B. Metson, *Phys. Chem. Chem. Phys.*, 2001, **3**,3838-3845.
- 34 I. Washio, Y. Xiong, Y. Yin, Y. Xia, *Adv. Mater.*, 2006, **18**, 1745-1749.
- 35 T. C. R. Rocha, D. Zanchet, *J. Phys. Chem. C*, 2007, **111**, 6989-6993.
- 36 J. Y. Liu, A. H. Hurt, *Environ. Sci. Technol.*, 2010, **44**, 2169-2175.
- 37 B. Zhang, J. Sun, C. Bi, G. Yin, L. Pu, Y. Shi, L. Sheng, *New J. Chem.*, 2011, **35**, 849-853.
- 38 Y. Fang, D. Gu, Y. Zou, Z. X. Wu, F. Y. Li, R. C. Che, Y. H. Deng, B. Tu, D. Y. Zhao, *Angew. Chem. Int. Ed.*, 2010, **49**, 7987-7991.
- 39 Y. Guo, H. S. Wang, C. L. He, L. J. Qiu, X. B. Cao, *Langmuir*, 2009, **25**, 4678-4684.